mathematics

MDPI

Article

Effect of Manufacturing Tolerances and Magnetic Anisotropy of Electrical Steel on Surface-Mounted Permanent Magnet Synchronous Motor Cogging Torque

Jae-Hyun Kim [1], Yun-Jae Won [2], Soo-Hwan Park [3] and Myung-Seop Lim [2,*]

[1] School of Mechanical Engineering, Yeungnam University, Gyeongsan-si 38541, Republic of Korea; jaehyun@yu.ac.kr
[2] Department of Automotive Engineering (Automotive-Computer Convergence), Hanyang University, Seoul 04763, Republic of Korea; w961227@hanyang.ac.kr
[3] Department of Mechanical, Robotics, and Energy Engineering, Dongguk University, Seoul 04620, Republic of Korea; parksh@dgu.ac.kr
* Correspondence: myungseop@hanyang.ac.kr

Abstract

Minimizing cogging torque is critical for surface-mounted permanent magnet synchronous motors (SPMSMs) in high-precision applications, such as electric power steering and robotics. While skewing techniques are typically applied to mitigate cogging torque, anomalous cogging torque harmonics frequently arise in mass production due to manufacturing tolerances and the inherent magnetic anisotropy of non-oriented electrical steel. This paper proposes a systematic analysis approach to distinguish the physical origins of these additional harmonics. By decoupling the effects of geometric and material properties, this study reveals that magnetic anisotropy interacts with slot harmonics to generate a distinct harmonic signature—specifically, the 16th-order harmonic for the 8-pole 12-slot SPMSM. Notably, 3D finite element analysis and experimental validation confirm that this anisotropy-induced cogging torque persists even after applying conventional step-skewing. These findings demonstrate that accounting for magnetic anisotropy is essential for the accurate prediction of cogging torque and the design of low-cogging-torque motors.

Keywords: cogging torque; manufacturing tolerance; non-oriented electrical steel; surface-mounted permanent magnet synchronous motor (SPMSM)

MSC: 65N30

Academic Editor: Udochukwu B. Akuru, Ogbonnaya I. Okoro and Yacine Amara

Received: 5 January 2026
Revised: 10 February 2026
Accepted: 11 February 2026
Published: 12 February 2026

1. Introduction

Surface-mounted permanent magnet synchronous motors (SPMSMs) are widely employed in high-precision applications, such as electric power steering and robotics, due to their high torque density and superior control performance [1–3]. However, minimizing cogging torque remains a critical design challenge, as it induces torque ripple, vibration, and acoustic noise, thereby degrading the control quality and user comfort [4]. Ideally, cogging torque appears at harmonics defined by the least common multiple of the pole and slot numbers. However, in mass production, the measured cogging torque often exhibits complex harmonic components that deviate from design predictions due to unavoidable manufacturing imperfections [5].

Extensive research has been conducted to identify the sources of these anomalous cogging torque harmonics, primarily focusing on manufacturing tolerances (MTs). The

sensitivity of cogging torque to various MTs has been investigated using analytical and finite element analysis (FEA) methods [6,7]. Regarding geometric asymmetries, it has been demonstrated that stator core roundness errors directly induce low-order cogging torque harmonics proportional to the deformation periodicity [8]. Similarly, rotor-side imperfections, such as permanent magnet (PM) placement errors and magnetization faults, have been identified to generate specific harmonic orders distinct from those caused by stator MTs [9–12]. To mitigate these sensitivities, various robust design optimization methods based on uncertainty characterization have been proposed [12–17]. Furthermore, recent studies have emphasized that manufacturing processes like punching and shrink fitting significantly degrade magnetic performance parameters, necessitating a comprehensive analysis of fabrication effects [18].

While geometric tolerances have been extensively studied, relatively less attention has been paid to the influence of material properties, specifically magnetic anisotropy. Although non-oriented electrical steel is widely used for its assumed isotropy, it inherently exhibits magnetic anisotropy due to the crystallographic texture developed during the rolling process [19,20]. It has been highlighted that tensile stress and processing conditions in non-oriented steel lead to significant variations in BH characteristics [21]. Several studies have attempted to model this anisotropy in FEA to predict the machine performance more accurately [22–24]. However, most of these studies have focused on iron loss reduction or average torque improvement, rather than identifying specific harmonic modulations in cogging torque [22–26]. In [22], a magnetic anisotropy model was proposed based on surface basis-cubic splines to accurately represent the BH characteristics of non-oriented steel sheets in FEA. In [23], a modified inverse vector hysteresis model was developed to describe anisotropic behavior under rotational excitations, focusing on the accuracy of the mathematical representation. Higuchi et al. [24] conducted a comparative study on modeling methods for 2D magnetic properties in synchronous machines, highlighting the advantages and disadvantages of various anisotropic models in terms of computational accuracy and cost. From an application perspective, research has primarily focused on efficiency improvement or average torque enhancement. In [25], the impact of the rolling direction in segmented stator cores was analyzed and the lamination arrangement was optimized to reduce core loss, rather than focusing on cogging torque quality. In [26], the performance of non-oriented and grain-oriented materials in axial flux machines was compared, demonstrating that anisotropic properties significantly affect the average torque and iron loss.

However, a critical limitation of these studies is that they primarily focus on the magnitude of performance metrics, such as total iron loss or average torque. They rarely investigate the specific harmonic modulation mechanism by which anisotropy interacts with slot harmonics to generate distinct anomalous cogging torque components. Consequently, even if these advanced models are used, it remains difficult to distinguish whether a specific harmonic peak observed in a mass-produced motor originates from material anisotropy or MTs without a detailed harmonic signature analysis. To address these issues, this paper investigates the independent and combined effects of MTs and magnetic anisotropy to identify the physical origins of additional cogging torque harmonics. Beyond simply applying a 3D FEA model, this study focuses on experimentally verifying that magnetic anisotropy generates a specific harmonic order that is distinct from those induced by geometric tolerances.

2. Additional Cogging Torque by Manufacturing Tolerances

In this section, the additional cogging torque harmonics resulting from MTs are analyzed. Four types of rotor MTs and two types of stator MTs, which significantly affect additional cogging torque, were investigated. For each MT, a total of 100 analysis points was determined randomly, assuming that the tolerance follows a normal distribution with

three standard deviations. To calculate the additional cogging torque harmonics, 2D electromagnetic FEA was performed. Since this study involves a statistical analysis requiring a large number of simulation cases, 2D analysis was chosen to maintain computational efficiency while sufficiently capturing the impact of geometric deviations on the planar magnetic circuit. The configuration of the target SPMSM used in this study is presented in Figure 1. Also, the detailed specifications and geometric parameters of the target model, including the stator and rotor dimensions, are listed in Table 1. For the core material, 50PN470 was used, which is a non-oriented electrical steel. The target model is an 8-pole 12-slot SPMSM, which ideally results in a 24th harmonic cogging torque. To eliminate this 24th harmonic cogging torque, a two-step-skew with a skew angle of 7.5° was applied. Figure 2 shows the cogging torque calculated by 2D FEA. As shown in Figure 2, the ideal peak-to-peak value of the nominal cogging torque is approximately 0.33 mNm, which corresponds to 0.016% of the rated torque listed in Table 1.

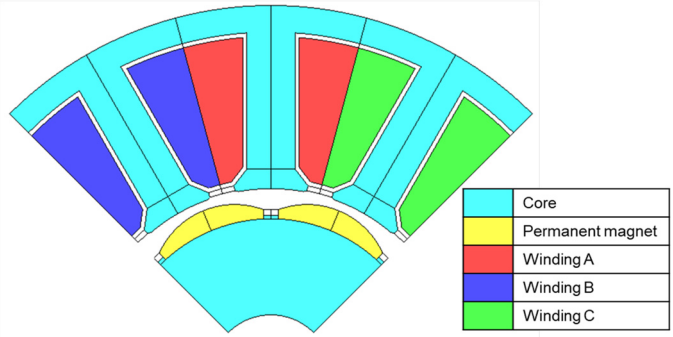

Figure 1. Configuration of the target 8-pole 12-slot SPMSM.

Table 1. Specifications of the target model.

Parameter	Value	Unit
Number of poles/slots	8/12	-
DC link voltage	12.0	V
Current limit	40.0	A_{rms}
Current density	15.0	A_{rms}/mm^2
Slot fill factor	45.0	%
PM residual induction	1.39	T
Stator outer diameter	86.0	mm
Stator inner diameter	47.4	mm
Air-gap length	1.0	mm
Tooth/Yoke width	5.85/3.25	mm
Slot opening width	4.0	mm
PM thickness	2.5	mm
Pole arc	39	degree
Step-skew angle	7.5	degree
Number of step-skew divisions	2	-
Stack length	18.0	mm
Rated speed	1000	rpm
Rated torque	2.1	Nm
Core material	50PN470	-

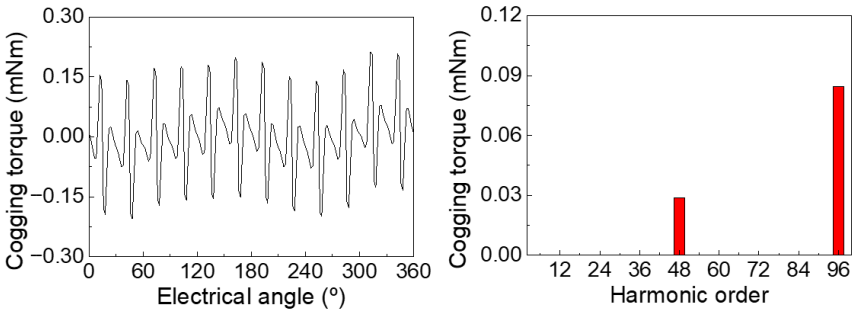

Figure 2. Cogging torque of the target model calculated by 2D FEA. (**a**) Waveform in one electrical period. (**b**) Harmonic analysis result in one mechanical period.

2.1. Additional Cogging Torque by Rotor Tolerances

The rotor MT types that significantly impact the cogging torque of the SPMSM were analyzed. Four types of rotor MTs were investigated, as follows:

1. Magnetization angle tolerance;
2. Bond thickness tolerance;
3. Permanent magnet (PM) thickness tolerance;
4. PM thickness difference between left and right sides.

These rotor MTs are illustrated in Figure 3, and the minimum and maximum ranges for each rotor MT type are summarized in Table 2. To evaluate the influence of each rotor MT type on cogging torque, 100 simulation cases were conducted using 2D electromagnetic FEA for each rotor MT type, as shown in Figure 4 (only the graph of magnetization angle tolerance is included due to space constraints). In Figure 4, PM1 through PM8 denote the eight individual PMs of the 8-pole rotor. In this study, to accurately emulate the stochastic nature of mass production, MTs were applied to all eight PMs simultaneously for each simulation case. Specifically, random deviation values were assigned to each PM independently within the specified tolerance range, rather than varying a single PM at a time. To determine the appropriate number of samples for the Monte Carlo analysis, a convergence test was performed. Figure 5 shows the variation in the standard deviation of the cogging torque with respect to the number of sampling points, analyzed for up to 300 cases. It was observed that the standard deviation for all tolerance factors stabilizes after approximately 100 points. Based on this convergence, 100 sampling points were selected as a sufficient sample size to ensure statistical reliability. Each rotor tolerance was assumed to follow a normal distribution, with maximum and minimum tolerances set to represent three standard deviations (3σ). When MT occurs in the rotor, additional cogging torque harmonics are generated in multiples of the slot number, as follows [5]:

$$\Delta T_{cog}(\alpha) = \frac{\pi l_{stk}}{4\mu_0}\left(R_2^2 - R_1^2\right)\sum_{n=1}^{\infty} nz\Delta F_{nz}\Delta\Lambda_n \sin(nz\alpha) \quad (1)$$

where $\Delta T_{cog}(\alpha)$ is the cogging torque at rotor position α, μ_0 is the vacuum permeability, l_{stk} is the stack length, and R_2 and R_1 denote the outer and inner radii of the air gap, respectively. The term n represents the harmonic order, and z is the number of slots. ΔF_{nz} and $\Delta\Lambda_n$ denote the Fourier coefficients of the magneto-motive force and the relative permeance, respectively.

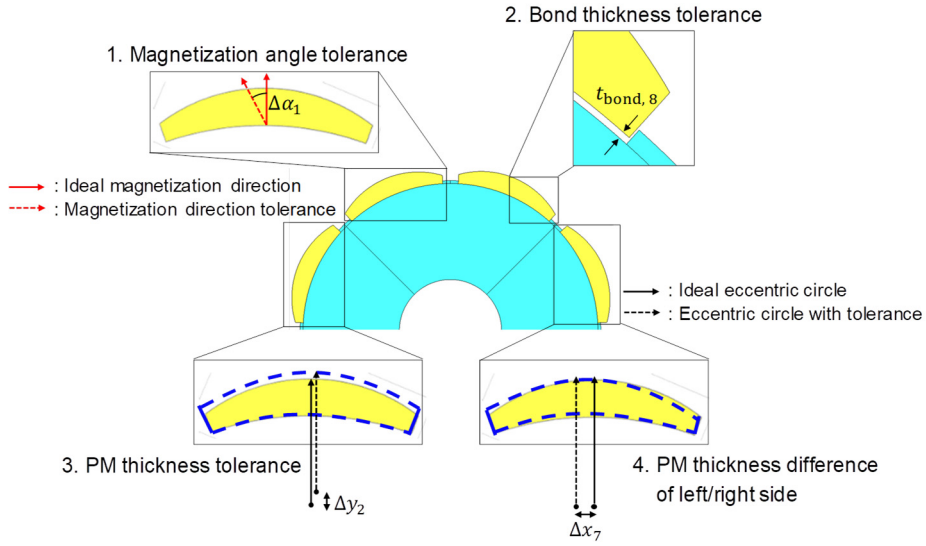

Figure 3. Manufacturing tolerances on the rotor.

Table 2. Ranges of rotor manufacturing tolerances.

Rotor Tolerance	Minimum	Maximum	Unit
Magnetization angle	−2	+2	degree
Bond thickness	0	+0.05	mm
PM thickness	−0.02	+0.02	mm
PM thickness difference between left and right sides	−0.04	+0.04	mm

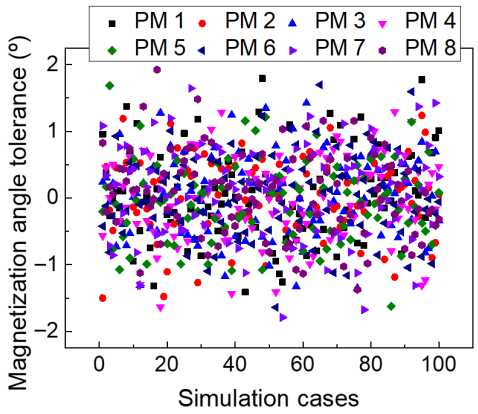

Figure 4. Simulation cases extracted to follow a normal distribution: Magnetization angle tolerance.

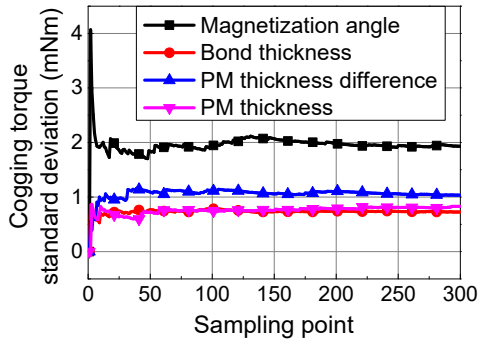

Figure 5. Variation in cogging torque standard deviation according to the number of sampling points for rotor MTs.

Accordingly, the 12th harmonic cogging torque was analyzed, and the histogram for each rotor MT type is shown in Figure 6. It can be seen that the rotor MTs can cause additional 12th harmonic cogging torque up to 4 mNm. Among the rotor MT types, the magnetization angle tolerance and the PM thickness difference between the left and right sides were found to have a significant impact on the 12th harmonic additional cogging torque. However, even after accounting for rotor MTs, no cogging torque was generated for other harmonic orders, such as the 8th, 16th, 24th, and 36th harmonics.

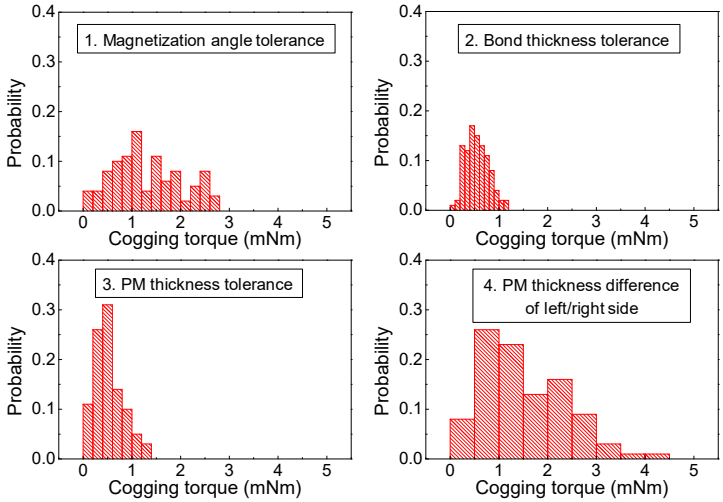

Figure 6. Histogram of the 12th harmonic cogging torque for each rotor MT type.

2.2. Additional Cogging Torque by Stator Tolerances

The stator MT types that significantly affect the cogging torque of the SPMSM were analyzed. Two types of the stator MTs were investigated, as follows:

1. Slot opening width tolerance;
2. Stator inner radius tolerance.

These stator MTs are illustrated in Figure 7, and the minimum and maximum ranges for each are summarized in Table 3. To evaluate the influence of each stator MT type on cogging torque, 100 cases were simulated using 2D electromagnetic FEA for each stator MT type. Each stator Mopic was assumed to follow a normal distribution, with maximum and minimum tolerances set to represent three standard deviations. Similarly, to justify the sample size for stator tolerances, the standard deviation of the cogging torque was analyzed with respect to the number of sampling points, as shown in Figure 8. The results indicate that the standard deviation converges after 100 cases. Therefore, 100 analysis points were determined to be statistically sufficient for investigating the stator MTs. When MTs occur in the stator, additional cogging torque harmonics are generated in multiples of the pole number, as follows [5]:

$$\Delta T_{cog}(\alpha) = \frac{\pi l_{stk}}{4\mu_0}\left(R_2^2 - R_1^2\right)\sum_{n=1}^{\infty} 2pnF_n\Delta\Lambda_{2pn}\sin(2pn\alpha) \quad (2)$$

where p is the number of pole pairs. Therefore, the 8th and 16th harmonic cogging torques were analyzed, and the histogram for each stator MT type is shown in Figure 9. It can be seen that the stator MTs can cause additional 8th harmonic cogging torque up to 8 mNm. Among the stator MT types, the stator inner radius tolerance was found to have a significant impact on the 8th harmonic additional cogging torque. However, even after accounting for stator MTs, cogging torque for other harmonic orders, such as the 16th harmonic, did not occur.

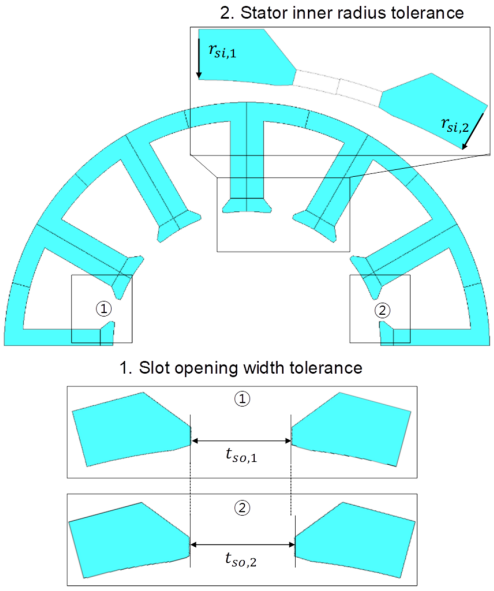

Figure 7. Manufacturing tolerances on the stator.

Table 3. Ranges of stator manufacturing tolerances.

Stator Tolerance	Minimum	Maximum	Unit
Slot opening width	0	+0.04	mm
Stator inner radius	−0.02	+0.02	mm

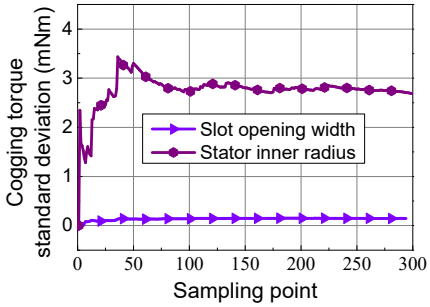

Figure 8. Variation in cogging torque standard deviation according to the number of sampling points for stator MTs.

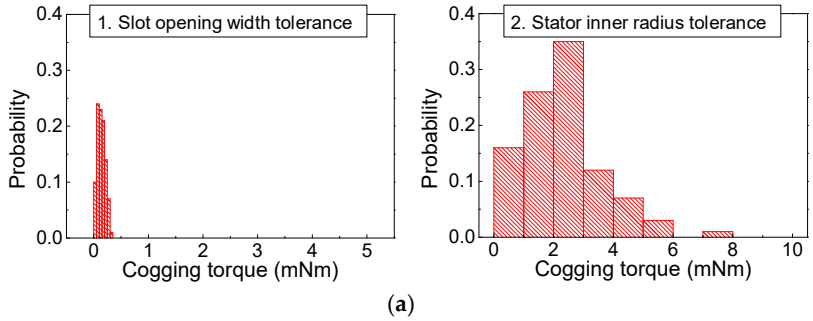

(**a**)

Figure 9. *Cont.*

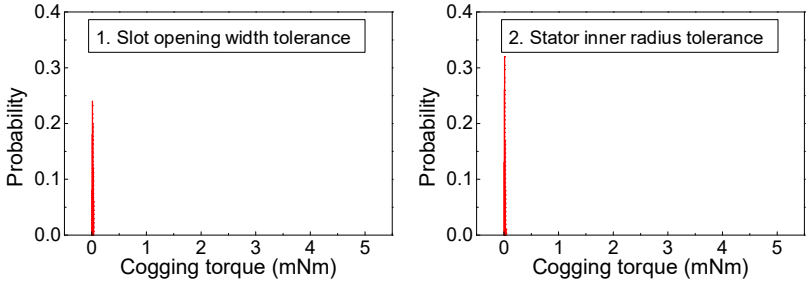

(**b**)

Figure 9. Histogram of the additional cogging torque for each stator MT type: (**a**) 8th harmonic, (**b**) 16th harmonic.

3. Effect of Anisotropy of Electrical Steel

In this section, the effect of the anisotropic property of non-oriented electrical steel on the cogging torque of SPMSMs was investigated. The RD refers to the longitudinal direction of the steel sheet manufactured during the rolling process, while the counter RD is the transverse direction perpendicular to the RD. Even in non-oriented electrical steel, there is a slight difference in saturation magnetic flux density between the RD and counter RD. This magnetic anisotropy is primarily caused by the crystallographic texture that inevitably forms during the cold-rolling process.

3.1. Analytical Derivation of Anisotropy Effect on Cogging Torque

To fundamentally analyze the generation of specific cogging torque harmonics due to anisotropy, a theoretical analysis based on the energy method was conducted. Neglecting the fringing effect and assuming infinite permeability of the iron core, the magnetic co-energy in the air gap can be calculated by integrating the magnetic energy density over the air-gap volume. Consequently, the cogging torque is derived as the derivative of the co-energy with respect to the rotor position, as follows:

$$T_{cog}(\alpha) = -\frac{\partial W(\alpha)}{\partial \alpha} = -\frac{l_{stk}\left(R_2^2 - R_1^2\right)}{4\mu_0}\frac{\partial}{\partial \alpha}\int_0^{2\pi} F^2(\theta,\alpha)\Lambda_{total}^2(\theta)d\theta \tag{3}$$

where $W(\alpha)$ represents the co-energy in the air gap, θ is the mechanical angle, and Λ_{total} is the total relative permeance. The squared magneto-motive force distribution can be expanded as a Fourier series involving the pole number, as follows:

$$F^2(\theta,\alpha) = F_0 + \sum_n^{\infty} F_n \cos\{2pn(\theta - \alpha)\} \tag{4}$$

Unlike MTs, which act as an additive perturbation to permeance, magnetic anisotropy acts as a multiplicative modulation on the stator permeance. Since the magnetic permeability varies with the rolling direction, the stator permeance can be expressed as the product of the slot permeance and the anisotropy function, as follows:

$$\Lambda_{total}(\theta) \approx \Lambda_{slot}(\theta) \cdot \Lambda_{aniso}(\theta) \tag{5}$$

$$\Lambda_{slot}(\theta) = \sum_k^{\infty} \Lambda_k \cos(kz\theta) \tag{6}$$

$$\Lambda_{aniso}(\theta) = 1 + \delta\cos(2\theta) \tag{7}$$

where $\Lambda_{slot}(\theta)$ is the relative permeance component due to the slotting effect, $\Lambda_{aniso}(\theta)$ is the relative permeance variation caused by magnetic anisotropy, and δ is the anisotropy coefficient, which quantifies the magnitude of permeance variation due to the material anisotropy. By substituting (5) into (3), the cogging torque generation is governed by

the squared permeance term. The squaring of the anisotropy term introduces a distinct harmonic modulation, as follows:

$$\Lambda_{total}^2(\theta) = \{\Lambda_{slot}(\theta) \times \Lambda_{aniso}(\theta)\}^2 \approx \left\{\sum_k^{\infty} \Lambda_k \cos(kz\theta)\right\} \cdot \{1 + \delta\cos(2\theta)\}^2 \quad (8)$$

$$\Lambda_{aniso}(\theta)^2 = 1 + 2\delta\cos 2\theta + \frac{\delta^2}{2}(1 + \cos 4\theta) \quad (9)$$

By substituting (4), (8), and (9) into (3), the integral is non-zero only when the harmonic orders match. The interaction between the fundamental slot harmonic (z = 12) in the slot permeance and the generated anisotropy harmonic (4th) creates a specific cogging torque component, as follows:

$$T_{cog}(\alpha) \propto \frac{\partial}{\partial\alpha}\sum_n^{\infty}\int_0^{2\pi} \cos\{2pn(\theta - \alpha)\} \cdot \{\cos 12\theta \cdot \cos 4\theta\} d\theta \quad (10)$$

According to the trigonometric product-to-sum rules, the term cos(12θ)·cos(4θ) generates spatial harmonics at orders 12 ± 4. For the 8-pole motor, the 16th harmonic component coincides with a multiple of the pole number, resulting in substantial 16th harmonic cogging torque. This derivation mathematically confirms that the 16th harmonic is a unique signature of anisotropy modulation.

3.2. Numerical Implementation of Magnetic Anisotropy

In this study, to quantitatively assess this effect, the saturation flux density in the counter RD was assumed to be 2% lower than that in the RD [19,27]. The magnetic anisotropy was implemented using an orthotropic magnetization model within the JMAG FEA framework. This model independently calculates the relationship between the magnetic field intensity H and the flux density B for each principal axis, as follows:

$$\begin{pmatrix} B_x \\ B_y \end{pmatrix} = \begin{pmatrix} \mu_{RD}(H) & 0 \\ 0 & \mu_{cRD}(H) \end{pmatrix} \begin{pmatrix} H_x \\ H_y \end{pmatrix} \quad (11)$$

where B_x, B_y and H_x, H_y are the magnetic flux density and magnetic field intensity components in the x- and y-directions, respectively. $\mu_{RD}(H)$ and $\mu_{cRD}(H)$ represent the magnetic permeability along the RD and counter RD, which are dependent on the magnetic field intensity. Based on typical characteristics of non-oriented electrical steel (e.g., 50PN470), where the saturation flux density in the counter RD is known to be 1% to 4% lower than in the RD [19,27], it was assumed the saturation magnetic flux density in the counter RD is 2% lower than that of the RD. Consequently, the nonlinear BH curve for the counter RD was modeled by scaling the flux density of the RD reference data by a factor of 0.98 across the entire magnetic field intensity range, as shown in Figure 10. By assigning these distinct directional properties, the spatial variation in magnetic reluctance was accurately represented to analyze the generation of additional harmonics.

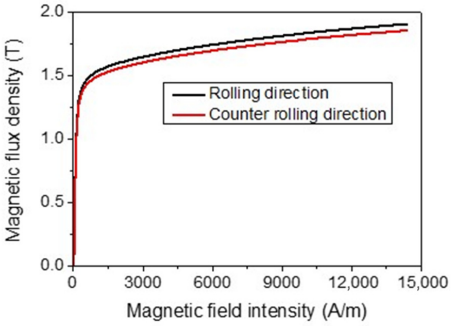

Figure 10. BH curve of non-oriented electrical steel according to the rolling direction.

3.3. Simulation Results and Analysis

To investigate the effect of this theoretical mechanism, 2D electromagnetic FEA was conducted, considering the anisotropic characteristics of non-oriented electrical steel. Since the magnetic anisotropy of non-oriented electrical steel is inherently a planar characteristic occurring within the lamination sheet, 2D analysis is sufficient to investigate the fundamental harmonic generation mechanism. The waveform and harmonic analysis results of the calculated cogging torque are shown in Figure 11. As can be seen, harmonic components at multiples of the pole number cogging torque occurred. Even when stator MTs were included in the analysis, the 16th harmonic cogging torque did not occur; however, after accounting for the anisotropic properties of the non-oriented electrical steel, the 16th harmonic cogging torque was generated.

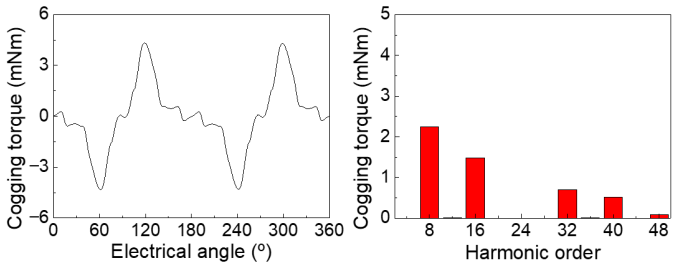

(**a**) (**b**)

Figure 11. Calculated cogging torque considering anisotropy characteristics of non-oriented electrical steel. (**a**) Waveform in one electrical period. (**b**) Harmonic analysis result in one mechanical period.

To analyze this, the magnetic flux density and permeability were investigated. Figure 12 shows the magnetic flux density contours with and without considering the anisotropic properties of non-oriented electrical steel. As can be seen, the saturation level of magnetic flux density increased slightly when anisotropic properties were considered, and the spatial distribution of magnetic flux density differed from the isotropic case. Since cogging torque is influenced by the spatial distribution of magnetic reluctance, this difference can result in the additional generation of a 16th harmonic cogging torque. Figure 13 shows the relative permeability at several positions based on the electrical angle. As shown in Figure 13a, relative permeability was calculated at four distinct positions, with the results presented in Figure 13b. Within one electrical cycle, the N and S poles of the PM complete one rotation, resulting in a two-period pattern in permeability. However, when the anisotropic properties of electrical steel are considered, the waveform of permeability contains many harmonic components, which results in 16th harmonic cogging torque generation.

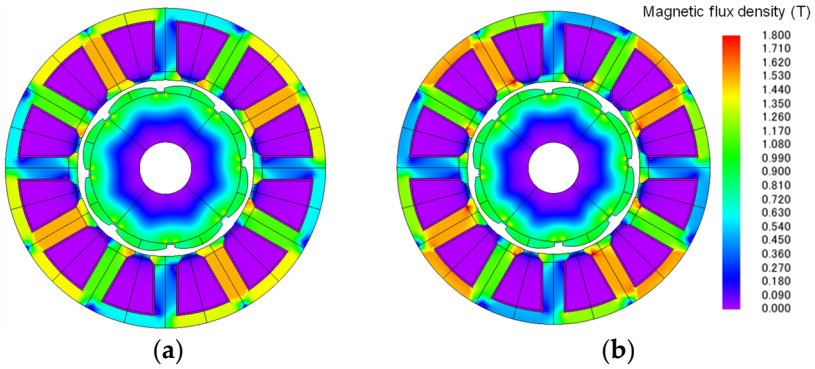

Figure 12. Magnetic flux density contour. (**a**) Without considering anisotropic properties. (**b**) Considering anisotropic properties.

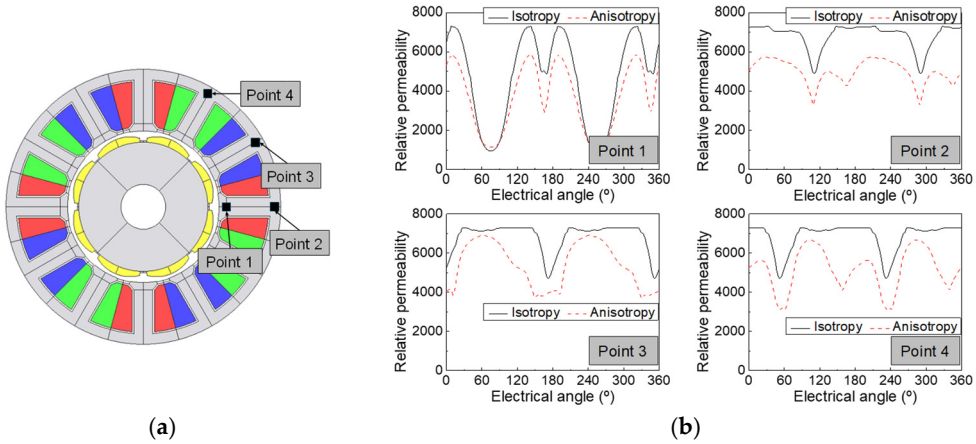

Figure 13. Relative permeability analysis results. (**a**) Analysis positions. (**b**) Waveform of relative permeability.

4. Validation Through Three-Dimensional FEA and Experiment

To validate the analysis results, a prototype was built, and the main MTs were measured, as shown in Figure 14. Figure 14a shows the fabricated stator and rotor of the prototype, while Figure 14b shows the MT measurement setup. To investigate the cause of the harmonic components in the measured cogging torque, the geometric deviations of the manufactured prototype were analyzed. The inner radius tolerance of each stator tooth and the bond thickness of the rotor for each PM were measured, and the results are shown in Figure 15. As shown in Figure 15a, the stator inner radius exhibits a non-uniform distribution across the teeth. This geometric unevenness indicates the presence of stator ovality and static eccentricity. These distortions break the symmetry of the magnetic circuit, creating additional flux harmonics that primarily contribute to the generation of the 8th harmonic cogging torque corresponding to the pole number. Figure 15b presents the measured thickness of the adhesive bond used for the PMs. The thickness varies significantly among the PMs. Since the recoil permeability of the PM is close to vacuum permeability, the variation in bond thickness has a limited effect on the total effective magnetic air-gap length. However, it causes the radial position of each PM surface to vary relative to the stator teeth. This positional deviation of the magnets interacts with the stator slot permeance, primarily contributing to the generation of the 12th harmonic cogging torque corresponding to the slot number.

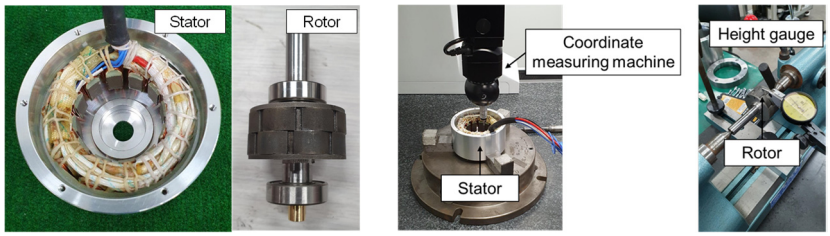

(**a**) (**b**)

Figure 14. Prototype stator and rotor. (**a**) Prototype. (**b**) Measurement setup.

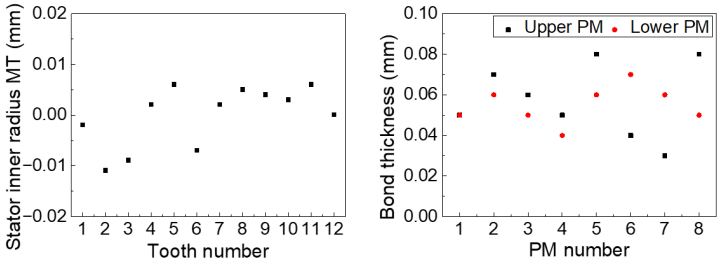

(**a**) (**b**)

Figure 15. Measured stator and rotor MTs. (**a**) Stator inner radius tolerance. (**b**) Rotor bond thickness.

Then, to confirm that the prototype adhered to the design specifications, the back electromotive force (BEMF) was measured and compared with the 3D FEA results, as shown in Figure 16. For the BEMF measurement, the line-to-line voltage was recorded using a high-performance digital oscilloscope (WaveRunner 64 Xi, Teledyne LeCroy 1049 Camino Dos Rios, Thousand Oaks, CA, USA) equipped with standard passive voltage probes. The measurement system features an 8-bit vertical resolution and a DC gain accuracy of 1.5%, which ensures sufficient precision for capturing the harmonic content. It can be seen that the measured and simulated BEMF at 1000 rpm were almost identical, indicating accurate fabrication of the prototype. Subsequently, the cogging torque was measured using a cogging torque meter. The test setup and measured cogging torque results are shown in Figure 17. The cogging torque measurement system is equipped with interchangeable torque sensors with capacities of 50 mNm to accommodate various torque ranges. In this experiment, the measurement was conducted at a fixed low speed of 1 rpm to ensure quasi-static conditions. The measurement accuracy of the system is within 1% for torque and approximately 1.5 degrees for the angular position. As can be seen, the measured cogging torque have many harmonic components, contrasting with the ideal cogging torque. The discrepancy between the ideal and measured results arises because the ideal model assumes perfect geometric symmetry and isotropic material properties. In the ideal case, the fundamental 24th harmonic is effectively suppressed by the rotor step-skew, resulting in negligible cogging torque. However, the actual prototype is subject to physical imperfections and 3D effects. First, geometric MTs, such as stator ovality and rotor magnetic imbalance, induce additional low-order harmonics (8th and 12th). Second, the magnetic anisotropy of the core material introduces specific sideband harmonics (8th and 16th). Third, 3D effects, including end-leakage flux and leakage flux between the step-skewed rotor segments, influence the results. In the actual PMSM, magnetic flux leaks between the adjacent skewed PMs and fringes at the stack ends. This leakage flux reduces the effectiveness of the step-skew in canceling harmonics, leading to residual cogging torque components that are not predicted in the ideal 2D analysis. These combined factors result in the complex waveform with multiple harmonic components observed in the measurement. To confirm the physical sources of these harmonics, specifically whether the additional

torque is caused by MTs or the anisotropic properties of non-oriented electrical steel, four types of 3D FEA were conducted as follows:

(1) Ideal case;
(2) Considering measured MTs and magnetization angle 2°;
(3) Considering anisotropic properties;
(4) Considering (2) and (3).

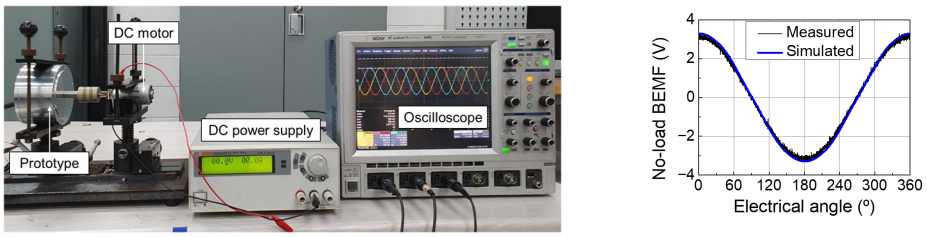

Figure 16. Test setup and results for measuring BEMF at 1000 rpm. (**a**) No-load test setup. (**b**) Measured and simulated BEMF.

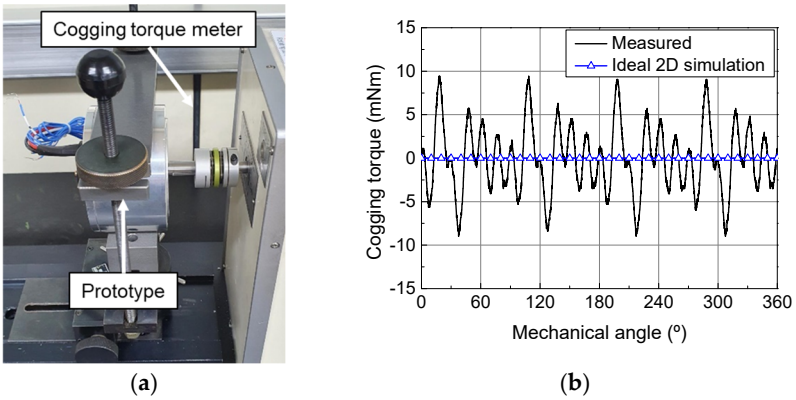

Figure 17. Test setup and results for measuring cogging torque. (**a**) Test setup. (**b**) Measured cogging torque.

The simulated cogging torques were compared with the measured cogging torque, as shown in Figure 18. As can be seen, in case (2), the 8th and 12th harmonic cogging torques occurred when stator and rotor MTs were considered. This is consistent with the geometric imperfections observed in Figure 15. However, the 16th harmonic cogging torque did not occur in case (2). because the high-order geometric error is negligible. The 16th harmonic cogging torque was generated only when the anisotropic properties of non-oriented electrical steel were included, as in cases (3) and (4). This confirms that the 16th harmonic is a unique signature generated by the modulation of magnetic anisotropy.

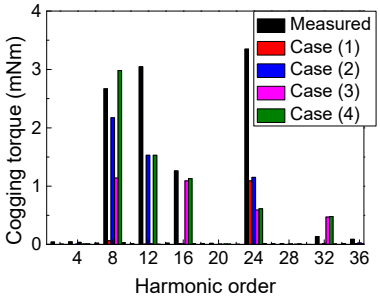

Figure 18. Measured and simulated cogging torque harmonic analysis results.

To quantitatively evaluate the accuracy of the simulation, the magnitudes of the dominant harmonic components for the measured data and simulation cases are summarized in Table 4. In case (2), which considers only MTs, the 8th and 12th harmonics were generated, whereas they were negligible in the ideal case (1). Specifically, the 8th harmonic in case 2 was calculated to be 2.17 mNm, accounting for a significant portion of the measured value. In contrast, case (3), which considers only magnetic anisotropy, shows a completely different trend. It generates a distinct 16th harmonic (1.09 mNm) comparable to the measured value, while generating negligible 12th harmonic torque. This clear separation confirms that the 16th harmonic is driven solely by magnetic anisotropy, whereas the 12th harmonic is driven by geometric tolerances. As shown in Table 4, case (4), which integrates both factors, achieves the best agreement. It captures the 8th and 16th harmonics with high accuracy. This validates that the MTs and magnetic anisotropy are indeed the dominant sources of these components. However, a significant discrepancy is observed for the 24th harmonic. This is because the 24th harmonic is the fundamental cogging torque, which the rotor step-skew is designed to eliminate. In the simulation, the step-skew effect is idealized, resulting in a nearly complete cancellation of the torque. In the actual prototype, however, leakage flux between the skewed magnet segments and end-leakage effects degrade the skew factor, resulting in a higher residual torque than predicted. Nevertheless, since the primary objective of this study is to identify the sources of the anomalous harmonics (8th, 12th, 16th), the high accuracy achieved for these specific orders confirms the validity of the proposed analysis. Therefore, case (4) showed the best agreement with the measurement, validating the analysis results.

Table 4. Comparison of measured and simulated cogging torque harmonics (unit: mNm).

Harmonic Order	Measured	Case 1	Case 2	Case 3	Case 4
8th	2.67	0.06	2.17	1.14	2.98
12th	3.05	0.01	1.53	0.01	1.53
16th	1.26	0.01	0.01	1.09	1.13
24th	3.35	1.09	1.15	0.59	0.61

The experimental results confirm that material properties play a crucial role in cogging torque generation mechanisms, aligning with observations in the existing literature. For instance, Kowal et al. [26] demonstrated that the anisotropic properties of electrical steel significantly affect the average torque and flux distribution in permanent magnet machines. Similarly, Leitner et al. [18], Zhang et al. [21], and Soda et al. [25] highlighted that manufacturing degradations, processing stresses, and rolling directions lead to non-negligible variations in magnetic performance. However, a distinct finding of this study, compared to previous works that primarily focused on the degradation of macroscopic parameters, is the identification of specific harmonic modulation. Our results reveal that the inherent anisotropy of non-oriented steel does not merely act as a broad noise factor but interacts with the slot harmonics to generate a distinct cogging torque component (the 16th harmonic for 8-pole 12-slot PMSM), which persists even after applying conventional reduction techniques like step-skewing.

5. Conclusions

This paper investigated the independent and combined effects of MTs and the magnetic anisotropy of non-oriented electrical steel on the cogging torque of SPMSMs. The primary findings revealed that geometric imperfections in the stator and rotor induce specific low-order harmonics, specifically the 8th and 12th orders, whereas the 16th-order harmonic is a

unique signature generated solely by the interaction between magnetic anisotropy and slot harmonics. Furthermore, experimental validation confirmed that this anisotropy-induced harmonic persists even after applying conventional step-skewing techniques. Based on these observations, it is concluded that relying solely on geometric tolerance management is insufficient for minimizing cogging torque in high-performance motors. The distinct harmonic signature identified in this study serves as a critical criterion for distinguishing material-induced faults from assembly errors, demonstrating that accurate cogging torque prediction requires a comprehensive analysis that considers not only MTs but also magnetic anisotropy. Regarding practical implications, this research suggests that motor designers must account for material anisotropy in the early design phase to ensure robustness. To mitigate the specific anisotropy-induced cogging torque harmonics, strategies such as reducing the implementation of rotational stacking of stator laminations are recommended.

Author Contributions: Conceptualization, J.-H.K. and S.-H.P.; methodology, J.-H.K.; validation, Y.-J.W.; formal analysis, Y.-J.W.; investigation, J.-H.K. and Y.-J.W.; writing—original draft preparation, J.-H.K.; writing—review and editing, J.-H.K. and M.-S.L.; visualization, J.-H.K. and S.-H.P.; supervision, M.-S.L.; project administration, J.-H.K.; funding acquisition, J.-H.K. All authors have read and agreed to the published version of the manuscript.

Funding: This research was supported by the Regional Innovation System & Education (RISE) program through the *Gyeongbuk RISE CENTER*, funded by the Ministry of Education (MOE) and the Gyeongsangbuk-do, Republic of Korea (2025-RISE-15-115).

Data Availability Statement: The original contributions presented in this study are included in the article. Further inquiries can be directed to the corresponding author.

Conflicts of Interest: The authors declare no conflicts of interest.

Abbreviations

The following abbreviations are used in this manuscript:

SPMSM	Surface-mounted permanent magnet synchronous motor
MT	Manufacturing tolerance
FEA	Finite element analysis
RD	Rolling direction
PM	Permanent magnet
BFMF	Back electromotive force

References

1. Won, Y.J.; Kim, J.H.; An, S.M.; Lim, M.S. Comparative Study of Cogging Torque, Torque Ripple, and Vibration on Stator Tooth Chamfer Types in Permanent Magnet Synchronous Motors. *IEEE Trans. Magn.* **2024**, *60*, 8202905. [CrossRef]
2. Kim, S.; Lee, S.G.; Kim, J.M.; Lee, T.H.; Lim, M.S. Robust Design Optimization of Surface-Mounted Permanent Magnet Synchronous Motor Using Uncertainty Characterization by Bootstrap Method. *IEEE Trans. Energy Convers.* **2020**, *35*, 2056–2065. [CrossRef]
3. Kim, J.-H.; Park, S.-H.; Ryu, J.-Y.; Lim, M.-S. Comparative Study of Vibration on 10-Pole 12-Slot and 14-Pole 12-Slot PMSM Considering Tooth Modulation Effect. *IEEE Trans. Ind. Electron.* **2023**, *70*, 4007–4017. [CrossRef]
4. Won, Y.J.; Kim, J.H.; Park, S.H.; Lee, J.H.; An, S.M.; Kim, D.Y.; Lim, M.S. Transfer Learning-Based Design Method for Cogging Torque Reduction in PMSM With Step-Skew Considering 3-D Leakage Flux. *IEEE Trans. Magn.* **2023**, *59*, 8204905. [CrossRef]
5. Ou, J.; Liu, Y.; Qu, R.; Doppelbauer, M. Experimental and Theoretical Research on Cogging Torque of PM Synchronous Motors Considering Manufacturing Tolerances. *IEEE Trans. Ind. Electron.* **2018**, *65*, 3772–3783. [CrossRef]
6. Ge, X.; Zhu, Z.Q. Sensitivity of Manufacturing Tolerances on Cogging Torque in Interior Permanent Magnet Machines with Different Slot/Pole Number Combinations. *IEEE Trans. Ind. Appl.* **2017**, *53*, 3557–3567. [CrossRef]
7. Jun, C.S.; Kwon, B.I.; Kwon, O. Tolerance Sensitivity Analysis and Robust Optimal Design Method of a Surface-Mounted Permanent Magnet Motor by Using a Hybrid Response Surface Method Considering Manufacturing Tolerances. *Energies* **2018**, *11*, 1159. [CrossRef]
8. Kitamura, M.; Enomoto, Y.; Kaneda, J.; Komuro, M. Cogging Torque Due to Roundness Errors of the Inner Stator Core Surface. *IEEE Trans. Magn.* **2003**, *39*, 1622–1625. [CrossRef]

9. Nakano, M.; Morita, Y.; Matsunaga, T. Reduction of Cogging Torque Due to Production Tolerances of Rotor by Using Dummy Slots Placed Partially in Axial Direction. *IEEE Trans. Ind. Appl.* **2015**, *51*, 4372–4382. [CrossRef]
10. Kim, J.M.; Yoon, M.H.; Hong, J.P.; Kim, S.I. Analysis of cogging torque caused by manufacturing tolerances of surface-mounted permanent magnet synchronous motor for electric power steering. *IET Electr. Power Appl.* **2016**, *10*, 691–696. [CrossRef]
11. Coenen, I.; van der Giet, M.; Hameyer, K. Manufacturing Tolerances: Estimation and Prediction of Cogging Torque Influenced by Magnetization Faults. *IEEE Trans. Magn.* **2012**, *48*, 1932–1936. [CrossRef]
12. Kim, K.S.; Jung, K.T.; Kim, J.M.; Hong, J.P.; Kim, S.I. Taguchi robust optimum design for reducing the cogging torque of EPS motors considering magnetic unbalance caused by manufacturing tolerances of PM. *IET Electr. Power Appl.* **2016**, *10*, 909–915. [CrossRef]
13. Lee, B.H.; Jung, J.W. Robust design for reducing cogging torque in surface-mounted permanent magnet synchronous motor considering tolerances of sub-components. *IET Electr. Power Appl.* **2020**, *14*, 448–456. [CrossRef]
14. Madariaga, C.; Jara, W.; Riquelme, D.; Bramerdorfer, G.; Tapia, J.A.; Riedemann, J. Impact of Tolerances on the Cogging Torque of Tooth-Coil-Winding PMSMs with Modular Stator Core by Means of Efficient Superposition Technique. *Electronics* **2020**, *9*, 1594. [CrossRef]
15. Liu, H.; Jin, X.; Bianchi, N.; Bramerdorfer, G.; Hu, P.; Zhang, C.; Yang, Y. A Permanent Magnet Assembling Approach to Mitigate the Cogging Torque for Permanent Magnet Machines Considering Manufacturing Uncertainties. *Energies* **2022**, *15*, 2154. [CrossRef]
16. Liu, C.; Lei, G.; Ma, B.; Guo, Y.; Zhu, J. Robust Design of a Low-Cost Permanent Magnet Motor with Soft Magnetic Composite Cores Considering the Manufacturing Process and Tolerances. *Energies* **2018**, *11*, 2025. [CrossRef]
17. Lee, S.G.; Kim, S.; Park, J.C.; Park, M.R.; Lee, T.H.; Lim, M.S. Robust Design Optimization of SPMSM for Robotic Actuator Considering Assembly Imperfection of Segmented Stator Core. *IEEE Trans. Energy Convers.* **2020**, *35*, 2076–2085. [CrossRef]
18. Leitner, S.; Gruebler, H.; Muetze, A. Effect of Manufacturing Influences on Magnetic Performance Parameters of Sub-Fractional Horsepower Motors. *IEEE Trans. Magn.* **2021**, *57*, 8205209. [CrossRef]
19. Cong, J.; Guo, F.; Qiao, J.; Qiu, S.; Wang, H. Optimum Magnetic Properties of Non-Oriented Electrical Steel Produced by Compact Strip Production Process. *Metals* **2022**, *12*, 64. [CrossRef]
20. He, Y.; Mehdi, M.; Hilinski, E.J.; Edrisy, A. Through-process characterization of local anisotropy of Non-oriented electrical steel using magnetic Barkhausen noise. *J. Magn. Magn. Mater.* **2018**, *453*, 149–162. [CrossRef]
21. Zhang, H.; Zeng, L.; An, D.; Pei, R. Magnetic Performance Improvement Caused by Tensile Stress in Equivalent Iron Core Fabricated by High-Strength Non-Oriented Electrical Steel. *IEEE Trans. Magn.* **2022**, *58*, 8600105. [CrossRef]
22. Martin, F.; Singh, D.; Rasilo, P.; Belahcen, A.; Arkkio, A. Model of Magnetic Anisotropy of Non-Oriented Steel Sheets for Finite-Element Method. *IEEE Trans. Magn.* **2016**, *52*, 7002704. [CrossRef]
23. Yue, S.; Anderson, P.I.; Li, Y.; Yang, Q.; Moses, A. A Modified Inverse Vector Hysteresis Model for Nonoriented Electrical Steels Considering Anisotropy for FEA. *IEEE Trans. Energy Convers.* **2021**, *36*, 3251–3260. [CrossRef]
24. Higuchi, S.; Takahashi, Y.; Tokumasu, T.; Fujiwara, K. Comparison Between Modeling Methods of 2-D Magnetic Properties in Magnetic Field Analysis of Synchronous Machines. *IEEE Trans. Magn.* **2014**, *50*, 7009104. [CrossRef]
25. Soda, N.; Hayashi, N.; Enokizono, M. Analytical Study on Core Loss Reduction of Segmented Stator Core Motor in Consideration of Rolling Direction of Nonoriented Electrical Steel Sheet. *IEEE Trans. Ind. Appl.* **2021**, *57*, 4745–4753. [CrossRef]
26. Kowal, D.; Sergeant, P.; Dupré, L.; Van den Bossche, A. Comparison of Nonoriented and Grain-Oriented Material in an Axial Flux Permanent-Magnet Machine. *IEEE Trans. Magn.* **2010**, *46*, 279–285. [CrossRef]
27. Chwastek, K. Anisotropic properties of non-oriented steel sheets. *IET Electr. Power Appl.* **2013**, *7*, 575–579. [CrossRef]